Tellus **000**, 000–000 (0000) Printed 27 September 2011 (Tellus LaTeX style file v2.2)

Data assimilation applied to a chaotic toy climate

By Kameron Decker Harris[1]*, El Hassan Ridouane[2], Darren L. Hitt[3], and Christopher M. Danforth[1]

[1] *Department of Mathematics and Statistics, Complex Systems Center, & the Vermont Advanced Computing Center, University of Vermont, Burlington, Vermont 05405, USA*

[2] *National Renewable Energy Lab, Golden, Colorado 80401-3305, USA*

[3] *Department of Mechanical Engineering, University of Vermont, Burlington, Vermont 05405, USA*

(27 September 2011)

ABSTRACT

A simplified model of natural convection, similar to the 1963 Lorenz system, is derived and compared to computational fluid dynamics simulations as a test bed for data assimilation methods. The thermosyphon is represented by a long time flow simulation, which serves as a reference "truth". Forecasts are then made using the Lorenz-like model and synchronized to noisy and limited observations of the truth, a realistic *in silico* forecasting scenario, using three dimensional variational filtering, the extended Kalman filter, the ensemble square root filter, and the ensemble transform Kalman filter. We find that these data assimilation algorithms successfully couple the simplified model to observations of the computational fluid dynamics simulation and, in fact, can infer dynamics absent from the model.

1 Introduction

Many of the problems associated with weather and climate forecasting do not result from our lack of knowledge of the governing geophysical equations. Even though such equations are well known, nonlinearities tend to amplify uncertainty in our estimate of the current atmospheric state, known as the initial condition (IC). In fact, even for a perfect IC, uncertainty in the parameters used to represent sub-grid scale phenomena (e.g. clouds in a global climate model) and other sources of model error lead to forecast divergence. Weather models define temperature, pressure, and other relevant quantities at regularly-spaced grid

* Corresponding author.

e-mail: kameron.harris@uvm.edu

© 0000 Tellus

points throughout the atmosphere, but meteorologists do not have observations at every one of these locations, so knowledge of the IC is inherently incomplete. To estimate the initial state of the atmosphere, statistically informed guesses are made for unmeasured variables. Over time, these guesses are validated by new measurements in a forecast-observe-analyze cycle called data assimilation (DA). Improving upon filters from control theory, modern DA techniques are used to estimate the best ICs for the short-term forecasts made by operational numerical weather prediction (NWP) models. However, DA is applicable to any modeling endeavor where only partial knowledge of the "truth" is available.

The *ensemble* forecasting methodology approximates uncertainty in the initial state with a finite set of perturbed ICs. The ensemble of ICs is integrated forward in time using the best available model; the resulting ensemble of forecasts estimates the probability distribution of potential outcomes. The ensemble spread quantifies forecast uncertainty, and the ensemble mean typically gives a better guess for the true state than any one member. However, the ensemble members must be chosen in a clever manner, because if the deviations of multiple ensemble members from the mean trajectory are linearly dependent, then the information they carry is redundant (Patil et al. (2001)). Furthermore, the number of degrees of freedom of modern NWP models is up to $\mathcal{O}(10^{10})$, so the numerical cost of integrating these models limits ensembles to $< \mathcal{O}(10^2)$ members in practical applications.

In this paper, we use a toy model for atmospheric convection to compare various methods of DA for prediction of nonlinear phenomena. The toy climate investigated is a thermosyphon, also known as a natural convection loop or non-mechanical heat pump. Thermosyphons are used in solar water heaters (Belessiotis and Mathioulakis (2002)), cooling systems for computers (Beitelmal and Patel (2002)), roads and railways that cross permafrost (Lustgarten (2006)), nuclear power plants (Detman and Whipp (1968); Beine et al. (1992); Kwant and Boardman (1992)), and other industrial applications. In the system, buoyant forces move fluid through a closed-loop with circular geometry (see Fig. 1). As the thermal forcing increases, the state of the thermosyphon undergoes a bifurcation from an initial purely conducting state to a steady convecting state. Under further forcing, steady convection becomes unstable and the flow reverses directions chaotically. As first suggested by Lorenz (1963), this system is illustrative of the unpredictable behavior observed in weather and climate dynamics.

Following previous experiments (Keller (1966); Welander (1967); Creveling et al. (1975); Gorman and Widmann (1984); Gorman et al. (1986); Ehrhard and Müller (1990)), we con-

Figure 1. The thermosyphon has a simple circular geometry. The bottom wall is heated to a constant hot temperature T_h while the top wall is maintained at the temperature T_c, creating a temperature inversion of hot fluid below cold fluid. If conduction alone cannot stabilize this temperature inversion, then the fluid will begin to rotate and convection becomes the dominant process of heat transfer. The most important model state variables are proportional to the bulk fluid velocity u and the temperature difference across the loop ΔT_{3-9}. For counterclockwise flow, as indicated by the arrow near 9 o'clock, $u > 0$ and ΔT_{3-9} is typically > 0. The radius ratio $R/r = 24$ used in our experiments is shown.

sider a circular thermosyphon geometry, analogous to a vertically-oriented hula hoop. An imposed wall temperature T_h on the lower half of the loop ($-\frac{\pi}{2} < \phi < \frac{\pi}{2}$) heats the fluid contained in this section. Similarly, a wall temperature $T_c < T_h$ is imposed on the upper half ($\frac{\pi}{2} < \phi < \frac{3\pi}{2}$) to cool the upper section (Fig. 1). The forcing is constant, i.e., we examine the case of developed flow and ignore transient behavior.

The behavior of the fluid can be qualitatively understood as follows. As fluid in the bottom of the loop heats past the point of simple conduction, buoyant forces overcome those of friction and viscosity, and the warm fluid rises (cool fluid sinks). The cyclical flow of hot and cold fluid forms a circular structure called a convection cell. Unlike Rayleigh-Bénard convection, in principle fluid in the thermosyphon is restricted to a single cell by the geometry and must initially rotate clockwise or counter-clockwise. The initial flow direction is determined randomly, since the symmetry of the tube's geometry and uniform heating do not favor any particular direction. The fluid will accelerate until the buoyant force is balanced by friction and gravity, and the flow stabilizes. With sufficient heating, i.e., large enough $\Delta T_w = T_h - T_c$, the laminar flow aperiodically reverses direction in a chaotic manner. This means that slightly perturbed states diverge exponentially in time. Among the goals of this research is to develop an accurate method for predicting when a flow reversal occurs, given a measurement time series of the volume-averaged mass flow rate.

This paper is structured in the following way: In Section 2, we explain the system of ODEs used for forecasting and the fluid dynamics simulation used to generate a synthetic true state or "nature run" of the toy climate. In Section 3, we explain DA, the *in silico* experiment, and discuss results. We conclude with implications for NWP in Section 4. Appendices S1 and S2 in Supporting Information detail the determination of model parameters and the DA methods used.

2 Description of Models

Several studies have examined the periodic (Keller (1966)) and chaotic (Welander (1967); Creveling et al. (1975); Gorman and Widmann (1984); Gorman et al. (1986); Ehrhard and

Müller (1990); Yuen and Bau (1999); Jiang and Shoji (2003); Burroughs et al. (2005); Desrayaud et al. (2006); Yang et al. (2006); Ridouane et al. (2009)) behavior of toroidal thermosyphons, many exhibiting behavior closely mimicking that of the Lorenz system (Lorenz (1963)). Gorman et al. (1986) developed a dynamical model for constant heat flux through the bottom half of the loop. A typical example of such a flux condition would be observed experimentally when the forcing is provided by a heating tape. Ehrhard and Müller (1990) derived similar equations of motion with fixed wall temperature for the top and bottom halves of the loop. We replicate these Dirichlet boundary conditions. One recent study used control theory to suppress chaotic behavior in both numerical and physical experiments (Yuen and Bau (1999)). Jiang and Shoji (2003) used a multiscale analysis of the field equations to derive simplified models for arbitrary boundary conditions. Burroughs et al. (2005) compared a partial differential equation model to three-dimensional (3D) direct numerical simulations; their model was able to determine the location of the various bifurcation points more accurately than the Lorenz equations, although they did not thoroughly investigate the chaotic behavior due to high computational cost. To our knowledge, Desrayaud et al. (2006) implemented the first two-dimensional (2D) direct numerical simulation of a thermosyphon. They were able to capture spatiotemporal details of the flow and found stable, periodic, and chaotic behavior. Ridouane et al. (2009) found similar results with a 2D numerical simulation and characterized the time-dependent structure of the flow immediately prior to a flow reversal. In the present study, we utilize this same flow simulation capability to establish the synthetic true state of the toy climate; computational details are presented in Section 2.2.

2.1 Ehrhard-Müller (EM) System

The dynamics of the thermosyphon are dominated by convection, resulting in Lorenz-like flow. By deriving the dynamical equations governing the thermosyphon from basic principles based on its geometry and the imposed boundary conditions, one is left with parameters in terms of physically meaningful constants and the scalings needed to make the state variables dimensionless. In principle, the physical properties of the fluid and loop define all parameters of the model. In practice, this is more complicated, because some parameters must be measured empirically (see Appendix S1 in Supporting Information).

2.1.1 Derivation Following the derivations of Gorman et al. (1986) and Ehrhard and Müller (1990), we consider the forces acting upon a control volume of incompressible fluid

in the loop. All fluid properties are cross-sectionally averaged, and the radial components of velocity and heat conduction within the fluid are neglected. The fluid velocity $u = u(t)$ is assumed to be constant at all points. Applying Newton's second law, the sum of all forces on the control volume must equal its change in momentum:

$$F_p + F_f + F_g = \rho\pi r^2 R d\phi \frac{du}{dt} \tag{1a}$$

where

$$F_p = -\pi r^2 R\, d\phi \nabla p = -\pi r^2 d\phi \frac{\partial p}{\partial \phi} \tag{1b}$$

$$F_f = -\rho\pi r^2 R\, d\phi\, f_w \tag{1c}$$

$$F_g = -\rho\pi r^2 R\, d\phi\, g \sin\phi\,. \tag{1d}$$

The angular coordinate ϕ and loop dimensions r and R are defined in Fig. 1; g is the acceleration of gravity, ρ is the fluid density, u is velocity, and p is pressure. The total force in Eqn. (1a) is comprised of the net pressure (F_p), friction from shear within the fluid (F_f), and the force of gravity (F_g). The pressure term, Eqn. (1b), is the volume times the pressure gradient. The friction term, Eqn. (1c), is written in this form in order to simplify the analysis; all frictional effects are contained in f_w which will depend on fluid velocity, to be discussed later.

Before we write the momentum equation, it is convenient to apply the Boussinesq approximation, which assumes that variations in fluid density are linear with temperature. In other words, $\rho = \rho(T) \approx \rho_0(1 - \gamma(T - T_0))$ where ρ_0 is the reference density, γ is the coefficient of volumetric thermal expansion, and $T_0 = \frac{1}{2}(T_h + T_c)$ is the reference temperature. The Boussinesq approximation also states that the density variation is insignificant except in terms multiplied by g. Thus, the density ρ is replaced by ρ_0 in all terms of Eqn. (1) except gravity, Eqn. (1d). Using the Boussinesq approximation, gathering terms, and dividing out common factors gives the momentum equation

$$\rho_0 \frac{du}{dt} d\phi = -d\phi \left(\frac{1}{R} \frac{\partial p}{\partial \phi} + \rho_0 \left(1 - \gamma(T - T_0)\right) g \sin\phi + f_w \right) . \tag{2}$$

Integrating about the loop, the momentum equation is simplified because u and f_w are independent of ϕ and other terms drop out due to periodicity.

$$\rho_0 \frac{du}{dt} = \frac{\rho_0 \gamma g}{2\pi} \int_0^{2\pi} d\phi\, T \sin\phi - f_w \tag{3}$$

We now must account for the transfer of energy within the fluid, and between the fluid and the wall. All modes of heat transfer are neglected except convection, which is a valid approximation when $r \ll R$ (Welander (1967); Ehrhard and Müller (1990)). The energy rate

of change (D/Dt is the material derivative with respect to time) in the control volume is

$$\rho_0 \pi r^2 R \, d\phi \, c_p \frac{DT}{Dt} \equiv \rho_0 \pi r^2 R \, d\phi \, c_p \left(\frac{\partial T}{\partial t} + \frac{u}{R} \frac{\partial T}{\partial \phi} \right) \tag{4}$$

which must be equal to the heat transfer through the wall

$$\Delta Q = -\pi r^2 R \, d\phi \, h_w (T - T_w) \,, \tag{5}$$

where c_p is the specific heat of the fluid, h_w is the heat transfer coefficient, which depends on velocity, and T_w is the temperature at the wall. Combining Eqns. (4) and (5) gives the energy equation

$$\left(\frac{\partial T}{\partial t} + \frac{u}{R} \frac{\partial T}{\partial \phi} \right) = -\frac{h_w}{\rho_0 c_p} (T - T_w) \,. \tag{6}$$

Together, Eqns. (3) and (6) represent a simple model of the flow in the loop.

The transport coefficients f_w and h_w characterize the interaction between the fluid and the wall. They are defined by the constitutive relations (Ehrhard and Müller (1990))

$$h_w = h_{w_0} \left[1 + K H(|x_1|) \right] \tag{7}$$

$$f_w = \frac{1}{2} \rho_0 f_{w_0} u \,, \tag{8}$$

where $x_1 \propto u$ is the dimensionless velocity. The function $H(x) = \Theta(1-x)p(x) + \Theta(x-1)x^{1/3}$ in Eqn. (7) determines the velocity dependence of the heat transfer coefficient, which varies as $u^{1/3}$ for moderate u (Ehrhard and Müller (1990)). We introduce the fitting polynomial $p(x) = 44/9\, x^2 - 55/9\, x^3 + 20/9\, x^4$ to ensure that h_w is analytic at $x_1 = 0$. The Heaviside step function $\Theta(x)$ causes $H(x)$ to vary as $p(x)$ for $x \leqslant 1$ and $x^{1/3}$ for $x > 1$. Eqn. (8) gives the frictional deceleration of the fluid when $|u| > 0$, and the $\rho_0/2$ term is retained to simplify the final solution. Dimensionally, f_w is an acceleration ($\mathrm{m/s^2}$) and h_w is power per unit volume per unit temperature ($\mathrm{W/m^3K}$). These coefficients h_{w_0}, f_{w_0}, and K must be estimated from experiments (e.g., Ehrhard and Müller (1990); Welander (1967); Gorman et al. (1986)) or from other empirical means. In Appendix S1 of Supporting Information, we describe the empirical methods used for parameter estimation.

Ehrhard and Müller (1990) solved the system of two coupled, partial differential equations (Eqns. (3) and (6)) by introducing an infinite Fourier series for T. The essential dynamics can be captured by the lowest modes, i.e.,

$$T(\phi, t) = C_0(t) + S(t) \sin\phi + C(t) \cos\phi \,. \tag{9}$$

Because this form of T separates the variables ϕ and t, the problem is transformed into a set of ordinary differential equations. Substituting Eqn. (9) into Eqn. (3) and integrating gives the equation of motion for u. Similarly, Eqn. (6) is integrated by $\oint d\phi \sin\phi$ and $\oint d\phi \cos\phi$ to

separate the two temperature modes S and C. The system is written in dimensionless form

$$\frac{dx_1}{dt'} = \alpha\,(x_2 - x_1) \tag{10a}$$

$$\frac{dx_2}{dt'} = \beta x_1 - x_2\,(1 + KH(|x_1|)) - x_1 x_3 \tag{10b}$$

$$\frac{dx_3}{dt'} = x_1 x_2 - x_3\,(1 + KH(|x_1|)) \tag{10c}$$

where the following linear transformations have been made to create dimensionless variables

$$\left.\begin{aligned} t' &= \frac{h_{w_0}}{\rho_0 c_p} t \\ x_1 &= \frac{\rho_0 c_p}{R h_{w_0}} u \\ x_2 &= \frac{1}{2}\frac{\rho_0 c_p \gamma g}{R h_{w_0} f_{w_0}} \Delta T_{3-9} \\ x_3 &= \frac{1}{2}\frac{\rho_0 c_p \gamma g}{R h_{w_0} f_{w_0}} \left(\frac{4}{\pi}\Delta T_w - \Delta T_{6-12}\right) . \end{aligned}\right\} \tag{11}$$

Physically, x_1 is proportional to the mean fluid velocity, x_2 to the temperature difference across the convection cell or ΔT_{3-9} (between 3 o'clock and 9 o'clock), and x_3 is proportional to the deviation of the vertical temperature profile (characterized by the temperature difference between 6 o'clock and 12 o'clock, ΔT_{6-12}) from the value it takes during conduction.

The parameter $\alpha = \frac{1}{2}\rho_0 c_p f_{w_0}/h_{w_0}$ is comparable to the Prandtl number, the ratio of momentum diffusivity and thermal diffusivity. Similar to the Rayleigh number, the heating parameter

$$\beta = \frac{2}{\pi}\frac{\rho_0 c_p \gamma g}{R h_{w_0} f_{w_0}} \Delta T_w \tag{12}$$

determines the onset of convection as well as the transition to chaotic behavior.

Although the previous derivation assumes a 3D geometry, the direct numerical flow simulations described in Section 2.2 were performed for the 2D case. A 2D geometry corresponds to infinite concentric cylinders as opposed to the quasi-1D torus. Due to cross-sectional averaging, the EM equations of motion (10) are the same in 2D or 3D; the change may be realized by letting $\pi r^2 \to 2r$ in Eqns. (1), (4), and (5) and carrying out the rest of the derivation. The only differences arise in the non-dimensional transformations and parameters, which were empirically determined by a multiple shooting algorithm (see Appendix S1 in Supporting Information).

The numerical integration of this autonomous ODE was performed, as is customary for the Lorenz system, with a fourth-order Runge-Kutta method and timestep 0.01 in MATLAB R2011b (2011).

2.1.2 Equilibrium Solutions The EM system exhibits two kinds of equilibrium solutions: a conductive steady state, located at the origin in state space and corresponding to no motion; and two convective steady states, corresponding to constant velocity in the clockwise or counterclockwise directions. Performing a linear stability analysis, these equilibrium states are found from the positive real root ξ^* of the equation

$$(\beta - 1) + (\beta - 2)KH(\sqrt{\xi}) - K^2H(\sqrt{\xi})^2 - \xi = 0 \tag{13}$$

which gives the convecting equilibria

$$\left[\pm\sqrt{\xi^*}, \pm\sqrt{\xi^*}, \xi^* / \left(1 + KH(\sqrt{\xi^*})\right)\right]^{\mathrm{T}}. \tag{14}$$

2.1.3 Flow Behavior As mentioned previously, the thermosyphon undergoes bifurcations from conduction to steady convection to chaotic convection (Welander (1967); Creveling et al. (1975); Gorman and Widmann (1984); Gorman et al. (1986)). For low β, stable conduction with a time-independent temperature field is the observed behavior. At a critical value of the heating parameter ($\beta = 1$, as for the Lorenz system), the two convective steady states bifurcate from the conducting equilibrium at the origin and become the attracting states for the system. These convecting equilibria move apart as β is increased, until they lose stability through a Hopf bifurcation and the system becomes globally chaotic. At slightly lower β, the system is subcritical, meaning there is the possibility of both chaotic and stable flows, depending on the IC (Gorman and Widmann (1984); Gorman et al. (1986)). Below the subcritical regime, the flow exhibits transient chaos which decays to stable oscillations or steady flow. Finally, it is worth noting that for very large values of the forcing, flow reversals cease to occur (Creveling et al. (1975); Gorman and Widmann (1984); Gorman et al. (1986)).

2.1.4 Relationship to Lorenz System Written in dimensionless form, the Lorenz (1963) equations read

$$\frac{dx}{dt} = s(y - x) \tag{15a}$$

$$\frac{dy}{dt} = rx - y - xz \tag{15b}$$

$$\frac{dz}{dt} = xy - bz. \tag{15c}$$

When $K = 0$, the EM system (Eqn. (10)) is analogous to the Lorenz system (Eqn. (15)) with $b = 1$. The lack of a geometric factor b in the EM system is due to the circular geometry of the

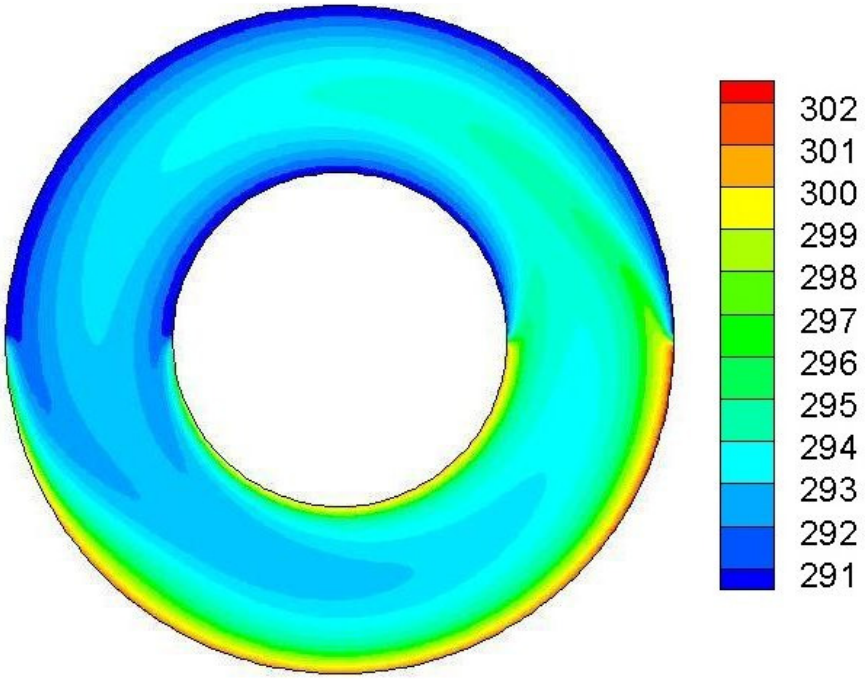

Figure 2. Flow simulation results showing the temperature profile, units of K, of steady counterclockwise convecting flow. The loop parameters are $\mathrm{Ra} = 1.2 \times 10^4$ and $R/r = 3$ (for visualization). In the chaotic case, time-varying antipodal regions of warmer and cooler fluid are superimposed on this temperature profile. As these pass through the loop, the "tongues" of warm and cool fluid extending into the top and bottom halves of the loop will grow and shrink simultaneously until the hot tongue visible near 2 o'clock reaches the opposite side of the loop. The flow then stalls and reverses direction.

convection cell. In Lorenz's derivation, the connection of the other dimensionless parameters to the thermosyphon design is not transparent. The Lorenz state variables x, y, and z are comparable to x_1, x_2, and x_3 in the EM system. The Lorenz equations have been widely used in nonlinear dynamics to study chaos and in NWP as a model system for testing DA (Miller and Ghil (1994); Yuen and Bau (1999); Annan and Hargreaves (2004); Evans et al. (2004); Yang et al. (2006); Kalnay et al. (2007)).

2.2 Computational Fluid Dynamics Simulations

In order to establish an independent reference of the thermosyphon state to which the EM model may be compared, 2D direct numerical simulations of the natural convective flow have been performed using computational fluid dynamics. The computational model used here has been described in detail in a previous study by Ridouane et al. (2009); however, for completeness, we summarize here its essential elements.

Consistent with the preceding modeling assumptions, temperature-dependent variations of material properties are regarded as negligible, save for the density ρ. The standard Boussinesq approximation is invoked and all fluid properties are assumed to be constant and

evaluated at the reference temperature $(T_h + T_c)/2$. The flow is assumed to be laminar, two-dimensional, with negligible viscous dissipation due to low velocities. Under these circumstances, the governing dimensionless equations are the unsteady, 2D laminar Navier-Stokes equations along with the energy equation. When cast in dimensionless form, the governing equations become:

$$\frac{\partial \rho}{\partial t} + \nabla \cdot (\rho \mathbf{u}) = 0 \tag{16}$$

$$\frac{\partial \mathbf{u}}{\partial t} + \mathbf{u} \cdot \nabla \mathbf{u} = -\nabla p + \mathrm{RaPr}\, T + \mathrm{Pr} \nabla^2 \mathbf{u} \tag{17}$$

$$\frac{\partial T}{\partial t} + \mathbf{u} \cdot \nabla T = \nabla^2 T \tag{18}$$

In the above equations $\mathbf{u}$ is the dimensionless velocity field and T is the dimensionless temperature. The length scale used in the non-dimensionalization is based on the loop thickness $2r$ and a diffusion time is used as a basis for temporal scaling. The quantities Ra and Pr are the Rayleigh and Prandtl numbers, respectively, introduced earlier in this article. Specifically, we set $\mathrm{Pr} = 5.83$, and the Rayleigh number is defined here as

$$\mathrm{Ra} = \frac{g \gamma \Delta T_w d^3}{\nu \kappa} \tag{19}$$

where g is the gravitational acceleration, γ is the thermal expansion coefficient, ν is the kinematic viscosity, κ is the thermal diffusivity, and ΔT_w is the temperature differential applied to the walls. For consistency with the previous study, the dimensions of the loop are chosen with $R = 36$ cm and $r = 1.5$ cm to yield a radius ratio of 24 (see Fig. 1). A computational mesh for this geometry consisting of $\approx 10^4$ elements has been previously shown to yield adequate spatial resolution for the simulations.

As in the classic Rayleigh-Bénard problem, the Rayleigh number determines the onset of convection in the thermosyphon. For the numerical simulations on this fixed geometry, a range of Rayleigh numbers can be imposed by varying the value of the gravitational acceleration. As the Rayleigh number is increased from zero, the flow behavior transitions from a stationary, conduction state to a steady, unidirectional state of convection. At still higher values of Ra, chaotic flow oscillations can be observed. Unless otherwise indicated, the simulation results presented in this paper correspond to a value of $\mathrm{Ra} = 1.5 \times 10^5$, which is within the chaotic regime.

The numerical simulations were performed using a finite-volume-based flow modeling software package Fluent 6.3 (2006). During the course of the simulations, flow monitors are used to record the time-varying mass flow rate within the system as well as the cross-

Figure 3. A cartoon of the DA process: When new observations are available, the analysis state is generated by combining observations with past forecasts. The analysis gives the optimal ICs for future forecasts. Ensemble methods do this with an ensemble of forecasts. After the initial spinup, analyses and forecasts should closely follow the truth.

sectional average temperatures at the $\phi = \pm\pi/2$ locations at 10 s intervals. In doing so, a synthetic time series of toy climate observations is recorded that can be used with the EM model in a forecasting scheme.

3 Methods and Results

3.1 Data Assimilation

DA is the process by which observations of a dynamical system are combined with forecasts from a model to estimate error covariances and calculate a "best guess" for the current state of the system, typically referred to as the *analysis*. This problem is difficult, because the forecaster uses an inexact forecasting model and never observes the true state of the dynamical system. The number of state variables in a NWP model is typically $\mathcal{O}(10^3)$ times the number of observations. Nevertheless, this best guess is used to produce a forecast, which is then used in the next assimilation cycle to fill in the blanks when new observations become available. Observations and forecasts are weighted depending on the confidence

in each, represented by error covariance matrices. A simplified version of the process is illustrated in Fig. 3.

A variety of filters are capable of solving the DA problem. The canonical example is the Kalman filter (KF), the optimal state estimation algorithm in a linear system. One of its first applications was to trajectory estimation and correction of missiles and rockets (Savely et al. (1972)). A number of nonlinear DA schemes are implemented in this study. In 3D variational DA (3D-Var; here 3D refers to the spatial dimensions for weather models), the background error covariance is estimated a single time, offline, prior to the data assimilation procedure. In the extended Kalman filter (EKF), it is evolved according to the linear tangent model, which approximates the evolution of small perturbations about the trajectory. Ensemble Kalman filters (collectively EnKFs) use ensembles of forecasts to estimate the background error. The methods examined in this study were 3D-Var, the EKF, the ensemble square root Kalman filter (EnSRF), and the ensemble transform Kalman filter (ETKF). Detailed descriptions of each method are included in Appendix S2 in Supporting Information.

3.2 Experimental Setup

A perfect model experiment, in which the Lorenz equations were used to forecast a synthetic truth created by that same system, was tested first. We found analysis errors similar to those reported by Yang et al. (2006) (3D-Var and EKF) and Kalnay et al. (2007) (ETKF), using the same model and tuning parameters.

In our more realistic scenario, as described in Section 2.2, the mass flow rate q and cross-sectionally averaged temperature at were reported during the course of numerical fluid simulations. The mass flow rate gave the fluid velocity $u = q/(2r\rho_0) \propto x_1$, since $2r$ is the 2D cross-sectional area. The temperature measurements were used to calculate $\Delta T_{3-9} \propto x_2$. The temperature data in our time series, however, were noisy. The EM model, in contrast with the simulated ΔT_{3-9} data, produces smooth x_2 trajectories. This is due to the simplifications of the EM model; the presence of a Kelvin-Helmholtz instability at the $\phi = \pm\pi/2$ boundary between heat source and sink is one source of these deviations from model behavior (Ridouane et al. (2009)). Assimilation of the scalar mass flow rate alone was sufficient for synchronization. Gaussian noise with standard deviation equal to 6×10^{-4} kg/s, approximately 0.8% of the mass flow rate climatological mean $\sqrt{\langle q^2 \rangle} \approx 0.076$ kg/s, was added to the synthetic truth to create observations.

When creating forecasts for the simulated thermosyphon with the EM model, the observations y of state variable q provide the only validation, so we calculate the forecast errors in observation space. These are given as root mean square error (RMSE), where RMSE $= \sqrt{\langle \delta q^2 \rangle}$. The residual at a specific assimilation cycle is given by $\delta q = q - \mathbf{H}\mathbf{x}^b$ where $\mathbf{x}^b$ is the background forecast and $\mathbf{H}$ is the linear observation operator described in Appendix S2 in Supporting Information. All errors are then scaled by $\sqrt{\langle q^2 \rangle}$, the climatology of q. Analysis error is a common metric for assessing model performance in perfect model experiments. In this study, however, we assert that background error is preferable. Analysis error in observation space, which can be small even for large assimilation windows, is not an appropriate metric for assessing model performance since it can disagree substantially with the background error. For example, 3D-Var in one experiment with a 10 minute assimilation window yielded analysis and background scaled errors of 0.08 and 0.86, respectively. The analysis error would seem to indicate that forecasting is doing a good job, but the background error shows that background forecasts are essentially meaningless. The filter, however, accounts for this and weights the observations heavily over the background forecasts when producing the analysis. Since we are concerned with forecasting, not reanalysis, background error is a more appropriate metric.

Model errors further complicate the implementation of DA in realistic forecasting scenarios. Usually, some type of covariance inflation is performed to prevent filter divergence. Kalnay et al. (2007) found that a Lorenz forecasting model with a slightly different forcing parameter ($r = 26$ versus $r = 28$) required a 10-fold increase in the multiplicative inflation factor when using a 3 member EnKF. Model error is more pronounced for our forecasts, since the EM model is a weaker approximation of the numerically simulated thermosyphon than the near-perfect model used in previous studies. We relied upon additive and multiplicative background covariance inflation to capture model error. Both types of inflation were required to prevent divergence of the EKF and EnKFs. Details of the inflation procedure and the parameters used are explained in Appendix S2 in Supporting Information.

All EM and DA parameter tuning was performed using a separate mass flow rate time series than was used for validation. Each DA algorithm was allowed 500 cycles to spinup, and its performance was measured over the following 2500 cycles. Ensemble size was set to 10 members.

Figure 4. Background RMSE scaled by $\sqrt{\langle q^2 \rangle}$ over 2500 assimilation cycles plotted for different DA algorithms and varying assimilation windows. As the window becomes larger, the error increases towards saturation. The lower dashed line in the main figure shows the limit of a "perfect" forecast while the upper demarcates a "useless" forecast (Kalnay, 2002).

3.3 Results

With proper tuning, all DA algorithms were capable of synchronizing the EM model to observations. As the assimilation window increased, scaled background error, the performance metric used, increased. See Fig. 4. For assimilation windows up to 2.5 min, all DA algorithms have indistinguishable errors. For assimilation windows between 3 and 6 min, 3D-Var performs noticably worse than the other methods which remain indistinguishable. Then, with assimilation windows greater than 6 min, the ensemble methods (EnSRF and ETKF) outperform the EKF noticably. This is perhaps surprising, because the ensemble size is significantly smaller than the dimension of the simulated thermosyphon state space ($\mathcal{O}(10^5)$ variables), although we know the thermosyphon dynamics effectively take place on a lower-dimensional manifold (the EM equations' attractor). EnKFs are known to outperform the EKF when the size of the ensemble exceeds the dimension of the state space.

Following the historical S1 score convention, scaled error above 70% is considered a "useless" forecast, while under 20% the forecast is "perfect" (Kalnay (2002)). Perfect forecasts for 3D-Var were found up to an approximately 4 minute assimilation window, while the other methods (EnSRF, ETKF, and EKF) produced nearly perfect forecasts with assimilation windows one full minute longer.

A persistent spike in background error for the 5 minute assimilation window (Fig. 4) is due to that time span being approximately the same as the characteristic period of oscillations in q (evident in Fig. 5(b)). This leads to a type of resonance in the DA-coupled EM system which degrades DA performance.

In Fig. 5 we show the results of the 3D-Var for 2, 5, and 10 min assimilation windows. The DA process is depicted in the same way as the schematic cartoon, Fig. 3, and background errors are also shown for each analysis cycle. The figure makes clear the degradation of forecast quality for larger assimilation windows. As the window length is increased, the background forecasts of q move farther from the true value. When the EM model erroneously predicts a flow reversal or lack thereof, the errors are largest.

Besides these quantitative results pertaining to forecast skill, we also found that the DA algorithms infer thermosyphon dynamics which are absent from the EM model. In Fig. 6 we see the simulated thermosyphon's attractor obtained by both a time-delay embedding

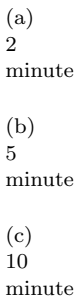

Figure 5. Results of 3D-Var assimilating the same data are shown for three different assimilation windows. The EM model states (background forecast and analysis) are transformed into observations of the mass flow rate q by the observation operator for comparison with the truth. In (a), observations are made frequently enough to keep the forecast close to the truth. In (b), the filter has satisfactory overall performance (scaled error $\approx 35\%$); note the error spike around 135 min when the forecast and truth end up in different flow directions. With the largest window (c), DA fails to keep the forecast state in the proper flow direction. The largest errors tend to occur at or near flow reversals due to inherent sensitivity near that transition and to the qualitatively different behavior of the different flow directions.

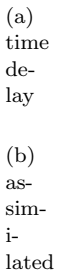

Figure 6. Two views of the numerically simulated thermosyphon attractor. A 60 s time-delay reconstruction, using the monitored mass flow rate, is shown in (a). In (b), plotted points show x_1 and x_2 of the EM analysis generated by EKF with an assimilation window of 120 s. Each is colored by the scaled forecast error at that point. Note how in (a) trajectories that move through the far edge of either lobe create distinctive loops near the center of the opposite lobe. This is an example of dynamics which are not present in the EM model without DA. It may explain the higher error for points in (b) at the far edge of each attractor lobe. See text for further description and Fig. 7 for another example.

(Fig. 6(a); Alligood et al. (1996)) and a projection of the EM analysis states (Fig. 6(b)). If the thermosyphon fluid flow stalls in the midst of a reversal, fluid in the bottom can quickly heat up while that in the top is cooled, leading to an unstable, strong temperature inversion. This causes the fluid to move very quickly in the reversed direction, but this new direction also ends up being unstable, and a new flow reversal can occur immediately. Absent DA, the EM model system does not exhibit this behavior of stalling followed by large swings of the trajectory.

In the time-delay embedding (Fig. 6(a)), this phenomenon is exhibited by loops in the trajectory as it moves near the convective fixed points. We emphasize that these are the convective fixed points. The flow stalls when the system state is near the conductive fixed point, then it swings wildly which brings it near the convective fixed point, but in such a way that it does not end up spiralling outward from there in the usual fashion as during a normal flow reversal. Instead, it quickly reverses again. Forecast skill is worst at the far edges

Figure 7. DA can infer dynamical behavior of the simulated thermosyphon absent from the EM model equations. Here we plot the EKF analysis, with a 30 s assimilation window, of the thermosyphon dynamics during a specific flow reversal. Points are colored by background scaled error. The trajectory, beginning at (a), stalls near the conducting equilibrium in the midst of a flow reversal, where it heats up significantly (b) before passing through two quick subsequent flow reversals (c-d) before resuming Lorenz-like behavior (e). See text.

of assimilated attractor (Fig. 6(b)), presumably during the wild swings of the EM trajectory after being ejected from the region of state space near the conducting equilibrium.

We also explicitly show one of these stalled flow reversals in Fig. 7, where we plot the EKF-assimilated EM trajectory using a 30 s assimilation window. When the fluid stalls, the x_3 variable moves closer to 0 (i.e. ΔT_{6-12} increases) while x_1 and x_2 (proportional to q and ΔT_{3-9}, respectively) are approximately 0, reflecting the growing inversion while the fluid remains stationary. When the fluid starts to move, the assimilated trajectory swings wildly to the right attractor lobe, then left, then right again before it settles into "normal" behavior, where the trajectory spirals outward from convecting equilibria between flow reversals. This contrasts the EM dynamics, for which large deviations in the system state from convecting equilibrium are driven close to the other convecting equilbrium during a flow reversal, which stabilizes the system. This result is present for all DA algorithms. The dynamics of and physics behind these regime changes will be the subject of a forthcoming companion paper.

4 Conclusions

DA was shown to be an effective way of coupling a simplified model to simulations of the toy climate. Although background forecast errors were always larger than observational noise, climatically scaled background error was small for reasonable assimilation windows. Proper tuning of multiplicative and additive inflation factors was essential for avoiding filter divergence and achieving low forecast error.

A laboratory thermosyphon device is in construction. The next stage of this research will apply similar methods to forecasting the system state, flow reversals, and flow direction durations using 3D numerical flow simulations. Spatial DA techniques, such as the LETKF (Kalnay et al. (2007); Hunt et al. (2007)), could be applied to finite-volume or finite-element models. These imperfect model experiments could be used to compare the relative performance of other DA algorithms (4D-Var; Kalnay et al. (2007)), synchronization approaches (adaptive nudging, see Yang et al. (2006)), and empirical correction techniques (Li et al. (2009); Danforth et al. (2007))

Although the thermosyphon is far from representing anything as complex and vast as

Earth's weather and climate, there are characteristics our toy climate shares with global atmospheric models. Sophisticated atmospheric models are, at best, only an approximate representation of the numerous processes that govern the Earth's climate. Global weather models and the EM model both parameterize fine-scale processes that interact nonlinearly to determine large-scale behavior. Clouds and precipitation are sub-grid scale processes in a global weather model, and the correlations for the heat transfer and friction coefficients are parameterizations of fluid behavior on a finer scale than can be dealt with in the derivation we have presented.

The methods we use to forecast the toy model are also similar to the methods used for global geophysical systems. Both require state estimation to find the IC from which to generate forecasts. Also, when forecasts are made in either system, the climatology is often more important than specific behavior: the occurrence of flow reversals for the thermosyphon; periodic behavior such as the El Niño Southern Oscillation, and statistics such as globally and regionally-averaged temperatures and their effects on rainfall, ice cover, etc. for climate. Each of these is a statistic that must be post-processed from the model output. To meet these global challenges, many techniques are needed in the modeling toolbox. In this way, toy models can provide us with insights that are applicable to the most important prediction problems of today.

Acknowledgments

We would like thank Dennis Clougherty, Peter Dodds, Nicholas Allgaier, and Ross Lieb-Lappen for comments and discussion. We also wish to acknowledge financial support from the Vermont Space Grant Consortium, NASA EPSCoR, NSF-DMS Grant #0940271, the Mathematics & Climate Research Network, and the Vermont Advanced Computing Center.

REFERENCES

Alligood, K. T., Sauer, T. D. and Yorke, J. A. 1996. Chaos: An Introduction to Dynamical Systems. Springer, New York.

Annan, J. D. and Hargreaves, J. C. 2004. Efficient parameter estimation for a highly chaotic system. *Tellus* **56A**, 520–526.

Beine, B., Kaminski, V. and Von Lensa, W. 1992. Integrated design of prestressed cast-iron pressure vessel and passive heat removal system for the reactor cell of a 200 MWth modular reactor. *Nuclear Engineering and Design* **136**, 135–141. 10.1016/0029-5493(92)90121-B.

Beitelmal, M. H. and Patel, C. D. 2002. Two-Phase Loop: Compact Thermosyphon, *Technical report*, HP Labs.

Belessiotis, V. and Mathioulakis, E. 2002. Analytical approach of thermosyphon solar domestic hot water system performance. *Solar Energy* **72**, 307–315. 10.1016/S0038-092X(02)00011-7.

Burroughs, E. A., Coutsias, E. A. and Romero, L. A. 2005. A reduced-order partial differential equation model for the flow in a thermosyphon. *Journal of Fluid Mechanics* **543**, 203–237.

Creveling, H. F., De Paz, J. F., Baladi, J. Y. and Schoenhals, R. J. 1975. Stability characteristics of a single-phase free convection loop. *Journal of Fluid Mechanics* **67**, 65–84.

Danforth, C. M., Kalnay, E. and Miyoshi, T. 2007. Estimating and Correcting Global Weather Model Error. *Monthly Weather Review* **135**, 281–299.

Desrayaud, G., Fichera, A. and Marcoux, M. 2006. Numerical investigation of natural circulation in a 2D-annular closed-loop thermosyphon. *International Journal of Heat and Fluid Flow* **27**, 154–166.

Detman, R. F. and Whipp, J. V. 1968, Thermosiphon deep pool reactor. US Patent #3393127.

Ehrhard, P. and Müller, U. 1990. Dynamical behaviour of natural convection in a single-phase loop. *Journal of Fluid Mechanics* **217**, 487–518.

Evans, E., Bhatti, N., Kinney, J., Pann, L., Peña, M., Yang, S.-C., Kalnay, E. and Hansen, J. 2004. RISE: Undergraduates Find That Regime Changes in Lorenz's Model are Predictable. *Bulletin of the American Meteorological Society* pp. 520–524.

Fluent 6.3. 2006. ANSYS, Centerra Resource Park, 10 Cavendish Court, Lebanon, NH 03766 USA

Gorman, M. and Widmann, P. J. 1984. Chaotic Flow Regimes in a Convection Loop. *Physical Review Letters* **52**, 2241–2244.

Gorman, M., Widmann, P. J. and Robbins, K. A. 1986. Nonlinear dynamics of a convection loop: a quantitative comparison of experiment with theory. *Physica D* **19**, 255–267.

Hunt, B. R., Kostelich, E. J. and Szunyogh, I. 2007. Efficient data assimilation for spatiotemporal chaos: A local ensemble transform Kalman filter. *Physica D* **230**, 112–126.

Jiang, Y. Y. and Shoji, M. 2003. Spatial and Temporal Stabilities of Flow in a Natural Circulation Loop: Influences of Thermal Boundary Condition. *Journal of Heat Transfer* **125**, 612–623.

Kalnay, E. 2002. Atmospheric Modeling, Data Assimilation and Predictability. Cambridge University Press.

Kalnay, E., Li, H., Miyoshi, T., Yang, S.-C. and Ballabrera-Poy, J. 2007. 4-D-Var or ensemble Kalman filter?. *Tellus* **59A**, 758–773.

Keller, J. B. 1966. Periodic oscillations in a model of thermal convection. *Journal of Fluid Mechanics* **26**, 599–606.

Kwant, W. and Boardman, C. E. 1992. PRISM–liquid metal cooled reactor plant design and performance. *Nuclear Engineering and Design* **136**, 111–120. `10.1016/0029-5493(92)90118-F`.

Li, H., Kalnay, E., Miyoshi, T. and Danforth, C. M. 2009. Accounting for Model Errors in Ensemble Data Assimilation. *Monthly Weather Review* **137**(10), 3407–3419. `10.1175/2009MWR2766.1`.

Lorenz, E. N. 1963. Deterministic Nonperiodic Flow. *Journal of the Atmospheric Sciences* **20**, 130–141.

Lustgarten, A. 2006. Next stop, Lhasa. *FORTUNE Magazine* **153**.

MATLAB. R2011b. The MathWorks, Inc, 3 Apple Hill Drive, Natick, MA 01760-2098 USA

Miller, R. N. and Ghil, M. 1994. Advanced Data Assimilation in Strongly Nonlinear Dynamical Systems. *Journal of the Atmospheric Sciences* **51**, 1037–1056.

Patil, D. J., Ott, E., Hunt, B. R., Kalnay, E. and Yorke, J. A. 2001. Local low dimensionality of atmospheric dynamics. *Physical Review Letters* **86**, 5878–5881.

Ridouane, E. H., Danforth, C. M. and Hitt, D. L. 2009. A numerical study of chaotic flow in a 2D natural convection loop. *Int. J. of Heat Mass Transfer* . `10.1016/j.ijheatmasstransfer.2009.10.003`.

Savely, R. T., Cockrell, B. F. and Pines, S. 1972. Apollo experience report – onboard navigational and alignment software, *Technical report*, NASA.

Welander, P. 1967. On the oscillatory instability of a differentially heated fluid loop. *Journal of Fluid Mechanics* **29**, 17–30.

Yang, S.-C., Baker, D., Li, H., Cordes, K., Huff, M., Nagpal, G., Okereke, E., Villafañe, J., Kalnay, E. and Duane, G. S. 2006. Data Assimilation as Synchronization of Truth and Model. *Journal of the Atmospheric Sciences* **63**, 2340–2354.

Yuen, P. K. and Bau, H. H. 1999. Optimal and adaptive control of chaotic convection — theory and experiments. *Physics of Fluids* **11**, 1435–1448.

Supporting Information

Additional supporting information may be found in the online version of this article:

Appendix S1. Model Parameter Estimation

Appendix S2. Data Assimilation Algorithms

Please note: Wiley-Blackwell is not responsible for the content or functionality of any supporting materials supplied by the authors. Any queries (other than missing material) should be directed to the corresponding author for the article.